Hindawi
Advances in Civil Engineering
Volume 2023, Article ID 8903428, 13 pages
https://doi.org/10.1155/2023/8903428

*Research Article*

# Acoustic Emission Characteristics and Damage Evolution of Sandstone with Different Pores under External Load

**Wencai Wang,[1] Junpeng Li,[1,2] Chuangye Wang,[1] and Zhenyu Pei[2]**

[1]*School of Mining and Coal, Inner Mongolia University of Science & Technology, Baotou 014010, China*
[2]*School of Energy Industry, Shanxi College of Technology, Shuozhou 036000, China*

Correspondence should be addressed to Junpeng Li; m15513345261@163.com

Received 4 November 2022; Revised 12 January 2023; Accepted 28 January 2023; Published 20 February 2023

Academic Editor: Jian Ji



The rock will be damaged and destroyed when the external load reaches the bearing limit, which will be accompanied by complex AE signals and damage evolution laws. Therefore, in order to obtain the relationship between AE signal and damage evolution characteristics of rocks, 4 kinds of sandstones of a mine are used for AE test. Firstly, the porosity of 4 kinds of sandstone is tested. Secondly, the AE signal parameter characteristics of sandstone with different porosity are analyzed. Finally, the AE parameters obtained are combined with cellular automata and damage theory to analyze the damage evolution law and critical damage value of different sandstones. The results show that the pore size of the four sandstones is $QSY_X > QSY_Z > FSY_X > FSY_Z$. The loading process is divided into compaction stage, elastic deformation stage, and plastic deformation stage, with peak strengths of 46.92 MPa, 43.32 MPa, 57.87 MPa, and 54.31 MPa, respectively. Or the AE event rate, the missing area, missing parts and missing number are different. The $QSY_X$ missing area is larger than $QSY_Z$ and $FSY_Z$; the macrocrack growth speed is also faster; and the signs of fracture are obvious. The number of $FSY_X$ missing is more than $QSY_X$, $QSY_Z$, and $FSY_Z$. The first two missing parts are caused by internal defects; the last two missing parts are signs of fracture; $QSY_X$, $QSY_Z$, and $FSY_Z$ are shear failure, and $FSY_X$ is tensile failure. The damage evolution process of the four sandstones corresponds to the loading process one by one. The calm stage of damage corresponds to the compaction stage, the damage expansion stage corresponds to the elastic deformation stage, and the damage acceleration stage corresponds to the plastic deformation stage. The critical damage values are 0.438, 0.499, 0.576, and 0.476, respectively, which are higher than the critical damage values of the sandstone cell model of 0.43, indicating that when the damage values reach the critical value, instability exists and instability failure will occur with continuous load.

## 1. Introduction

Acoustic emission (AE) technology refers to the phenomenon that rock materials generate transient elastic waves with rapid energy release under external load [1, 2]. As a combination of micro elements in geotechnical engineering, the AE signal displayed in the loading process of rock can well reflect the evolution process and damage degree of microcrack initiation, propagation and penetration, which has led many scholars to do a lot of research work [3–6]. Lockner [7] analyzed the failure mechanism and shape of rock through acoustic emission technology. Manthei [8] studied the rock failure characteristics through acoustic emission technology, and concluded that the overall change trend of acoustic emission signal characteristics received by low frequency and high frequency channels in the process of rock fracture is basically the same. Lu et al. [9] tested the coal rock mixture sample with rockburst tendency through compression test, and found that with the increase of load, the main frequency of acoustic emission transits to the low frequency band. When rockburst occurs, the lower the main frequency, the higher the corresponding acoustic emission energy, and the more violent the rockburst. Zhang et al. [10] has tested and analyzed the spatial distribution of acoustic emission of salt rock, granite and marble through compression test, and concluded that the spatial distribution of acoustic emission events is concentrated in areas corresponding to fracture areas. Yang and Jing [11] analyzed the impact of crack aggregation on the damage

degree and deformation and failure behavior of brittle sandstone containing cracks through AE event rate and energy rate, and concluded that the damage evolution process of brittle sandstone is divided into initial damage stage, damage stable devel-opment stage and damage accelerated development stage. Eberhardt et al. [12] characterized the damage from the acoustic emission event rate and ringing, and studied the damage evolution law of rock, and concluded that the damage and failure of rock mainly occurred in the plastic deformation stage. Erarslan and Williams [13] conducted acoustic emission tests on homogeneous and precracked rocks through numerical simulation method, and concluded that both precracks and new cracks under load will affect the stress distribution of the test piece. Li and Wong [14] established a three-dimensional homogeneous linear elastic model of microcrack development based on the rock acoustic emission test, and concluded that the stress distribution along the thickness of the specimen under load is not uniform but symmetrical. Invernizzi et al. [15] studied the rock cracking mode and size effect through uniaxial compression test, and obtained a good correlation between the number of acoustic emission signals and the fracture bond between particles. Zhang and Deng [16] proposed a new method to determine the optimal transition line for crack classification in acoustic emission parameter analysis based on the dominant frequency characteristics of acoustic emission signals. This method can determine the ratio and prediction ratio of tensile cracks and shear cracks, providing a new idea for rock fracture classification. Wu et al. [17] conducted acoustic emission tests on sandstone, granulite, granite and limestone. Taking time as the intermediate variable, they established a relationship model between acoustic emission ringing count and strain. Based on the Weibull distribution damage constitutive model, they derived the relationship between acoustic emission ringing count and damage variable. Gu et al. [18] study the mechanical behaviors and AE characteristics of fractured coals, elucidated the influence of primary cracks on the strength of brittle coal specimens containing preexisting fissures and the mechanical behavior and failure mechanism in underground engineering.

Through the above analysis, scholars' understanding of acoustic emission signal characteristics and damage evolution process of rock under external load is enhanced, which lays a solid foundation for the study of rock fracture mechanism. Based on this, on the basis of the above achievements, this research introduces cellular automata theory to analyze the acoustic emission evolution characteristics and the determination of damage critical value of sandstone with different pores, and comprehensively analyzes the acoustic emission parameter characteristics and the evolution process of fracture morphology of sandstone with different pores. This can lay a foundation for the follow-up engineering rock stability research and evaluation.

## 2. Testing Overview

*2.1. Sample Preparation.* The Materials and Methods should be described with sufficient details to allow others to replicate and build on the published results. Please note that the publication of your manuscript implicates that you must make all materials, data, computer code, and protocols associated with the publication available to readers. Please disclose at the submission stage any restrictions on the availability of materials or information. New methods and protocols should be described in detail while well-established methods can be briefly described and appropriately cited.

Research manuscripts reporting large datasets that are deposited in a publicly available database should specify where the data have been deposited and provide the relevant accession numbers. If the accession numbers have not yet been obtained at the time of submission, please state that they will be provided during review. They must be provided prior to publication.

Interventionary studies involving animals or humans, and other studies that require ethical approval, must list the authority that provided approval and the corresponding ethical approval code.

The sandstone required for this test comes from a large open-pit mine, and 0.6 $m^3$ is taken for each type. Samples with a diameter of 50 mm and a height of 100 mm are taken under the condition of avoiding the cracks and structures of the original rock, and the two ends are ground flat to an unevenness of less than 0.05 mm, and the deviation of the section perpendicular to the axis is less than 0.25°. There are 12 sandstone samples, $QSY_{X1}$, $QSY_{X2}$ and $QSY_{X3}$ are fine green sandstone, $QSY_{Z1}$, $QSY_{Z2}$ and $QSY_{Z3}$ are medium green sandstone, $FSY_{X1}$, $FSY_{X2}$ and $FSY_{X3}$ are fine siltstone, $FSY_{Z1}$, $FSY_{Z2}$ and $FSY_{Z3}$ are medium siltstone as shown in Figure 1.

*2.2. Test Method and Parameter Setting.* Newmai Minim-60 MRI scanner and electro-hydraulic servo rock testing machine were used to detect the porosity of different sandstones and conduct uniaxial compression acoustic emission test.

(1) After saturated water absorption of different sandstone samples, the samples are put them into the sample detection equipment, the received signals are output through the signal receiving equipment, and $T_2$ spectrum is drawn;

(2) After both sides of the specimen to be tested are coated with uniform couplant, one acoustic emission probe is fixed in the extensometer and the test machine is operated to make the specimen rise close to the loading platform. Set the parameters of the test machine (preload 2 kN, loading rate 0.1 mm/min) and acoustic emission parameters (sampling frequency 100 kHz, sampling length 2,048, waveform threshold 40 dB, parameter threshold 40 dB, amplifier gain 40 dB).

(3) After parameter setting, operate the testing machine and acoustic emission system at the same time to make them run synchronously until the sample breaks. Turn off the testing machine and acoustic emission system, take out the broken sample, place it and extract the collected data, and export them for future use.


Figure 1: Original sandstone samples with different pores.

## 3. Analysis of Test Results and Morphological Deterioration Characteristics of Sandstone with Different Porosity

*3.1. Analysis of Porosity Characteristics of Different Sandstones.* According to the analysis of mineral composition, rocks are cemented by particles with different sizes and shapes. Pores will be formed during the molding process. Relevant studies call this porosity, which refers to the percentage of the pore volume of rocks and the total volume of rocks in natural state, and is the embodiment of the density of rock materials.

After different sandstone samples are saturated with water, the internal pores will be filled with water molecules. During NMR detection, H protons in the pore fluid will absorb electromagnetic energy under the action of an external magnetic field, which will generate a large number of energy signals. This phenomenon is called relaxation, including volume relaxation, surface relaxation and diffusion relaxation. Relevant literature [19] express the lateral relaxation rate of NMR as:

$$\frac{1}{T_2} = \frac{1}{T_{2\text{freefluid}}} + \rho^2\left(\frac{S}{V}\right)_{\text{pore}} + \frac{D(\gamma G T_E)^2}{12}. \quad (1)$$

It can be seen from literature that the surface relaxation of the sample pores during NMR testing is larger than the other two types of relaxation, so formula (1) can be simplified as:

$$\frac{1}{T_2} = \rho^2\left(\frac{S}{V}\right)_{\text{pore}} = +\frac{F_S\rho^2}{r}. \quad (2)$$

In the above two formula, $T_{2\text{freefluid}}$ represents free relaxation time of fluid (ms), $S$-represents pore surface area ($\text{cm}^2$), $\rho_2$-represents transverse surface relaxation strength ($\mu$m/ms); $D$-represents diffusion coefficient, $\gamma\gamma$-represents gyromagnetic ratio (rad/(ST), $G$-represents magnetic field gradient (Gs/cm), $T_E$-represents echo time (ms), $F_S$-represents geometry factor, $r$-means pore radius (cm).

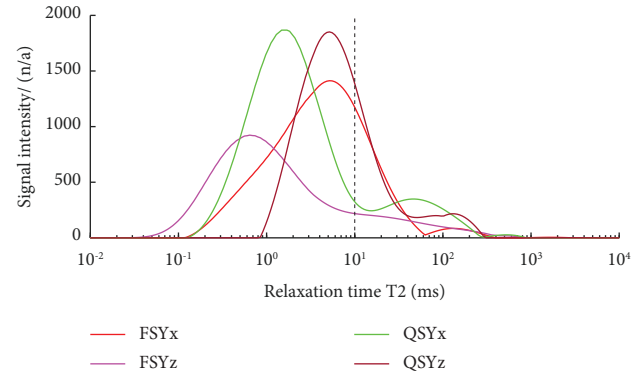


Figure 2: $T_2$ spectrum of original sandstone samples.

It can be seen from formula 2 that the size of rock pores is directly proportional to the distribution. Relevant scholars [19] divide the size of pores into small pores and large pores based on the benchmark of $T_2 = 10$ ms. When $T_2 < 10$ ms, they are small pores. When $T_2 > 10$ ms, they are large pores. The larger the signal intensity, the more the number of pores corresponding to $T_2$. Therefore, on the basis of NMR detection, $T_2$ spectra of four different sandstone samples can be obtained, as shown in Figure 2.

It can be seen from Figure 2 that the $T_2$ distribution interval of $\text{QSY}_X$, $\text{FSY}_X$ and $\text{FSY}_Z$ is between $10^{-1}$ and $10^3$ ms, and that of $\text{QSY}_Z$ is between 10 and $10^3$ ms, which indicates that the large and small pores of $\text{QSY}_X$, $\text{FSY}_X$ and $\text{FSY}_Z$ coexist, and the $\text{QSY}_Z$ is dominated by large pores; The $T_2$ distribution of the four sandstones is unimodal, the peak interval of $\text{QSY}_X$ and $\text{FSY}_Z$ is $10^{-1}$~10 ms, and the peak interval of $\text{QSY}_Z$ and $\text{FSY}_X$ is $10^0$~10 ms. According to the peak position, it can be determined that $\text{QSY}_X$ pores are smaller than $\text{QSY}_Z$, and $\text{FSY}_X$ pores are smaller than $\text{FSY}_Z$ pores; $\text{FSY}_X$ signal strength value is less than 1,500 n/a, $\text{FSY}_Z$ signal strength value is less than 1,000 n/a, $\text{QSY}_X$ and $\text{QSY}_Z$ signal strength values are between 1,500 n/a and 2,000 n/a, and $\text{QSY}_X$ is greater than $\text{QSY}_Z$. According to the signal strength value, it can be determined that $\text{QSY}_X$'s pore is greater than that of $\text{FSY}_X$, and $\text{QSY}_Z$'s pore is greater than that of $\text{FSY}_Z$. It can be seen that the pore size distribution of the four sandstone samples is $\text{QSY}_Z > \text{QSY}_X > \text{FSY}_Z > \text{FSY}_X$ in order, and the pore size of the four samples measured by the weighing method (Table 1) is consistent with the above analysis.

*3.2. Analysis of AE Test Results of Sandstone with Different Pores under External Load*

*3.2.1. Time-Stress Analysis of Sandstone with Different Pores.* Since the parameters such as stress-time and AE signal of the samples of the same lithology under external load are relatively consistent, one sample is taken for analysis when the length is fixed.

It can be seen from Figure 3 that axial stress-time is used as a visual analysis curve to reveal rock stress failure under external load, and its characteristic distribution is as follows:

(1) The axial stress of the four sandstones is negatively correlated with the pore size. The larger the pore, the

Table 1: Nuclear magnetic porosity test results of sandstone with different pores.

| Lithology | Volume ($cm^3$) | Semaphore | Porosity (%) |
|---|---|---|---|
| $QSY_X$ | 196.25 | 1,867 | 3.92 |
| $QSY_Z$ | 196.25 | 1,826 | 4.34 |
| $FSY_X$ | 196.25 | 1,413 | 3.01 |
| $FSY_Z$ | 196.25 | 924 | 3.64 |

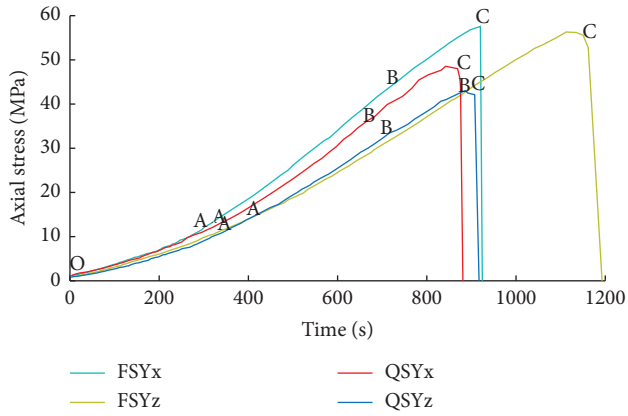


Figure 3: Axial stress-time curve of sandstone samples.

smaller the axial stress. The stress values are 46.92 MPa, 43.32 MPa, 57.87 MPa and 54.31 MPa respectively;

(2) The stress-time curves of the four sandstones can be divided into three stages: I (compaction stage, OA section), II (elastic deformation stage, AB section) and III (plastic deformation stage, BC section), of which the compaction stage and failure and instability stage last a short time, and the fracture derivation and expansion stage lasts a long time. All belong to elastic-plastic deformation, and the failure mode is brittle failure.

*3.2.2. Analysis of AE Event Rate and Cumulative Event Number of Sandstone with Different Pores.* In the acoustic emission test, the AE event rate-cumulative event number change of rock during the loading process is essentially the dynamic response characteristics displayed in the stage time, and these characteristic signals can reflect the laws and phenomena of rock deformation and deterioration [20].

AE event rate refers to the number of AE events in a unit time. The cumulative event number is the accumulation of the total number of events from the initial load to the fracture stage. Combining the above two parameters with stress time, the AE event rate - cumulative event number-axial stress evolution relationship diagram of four kinds of sandstone can be drawn, as shown in Figure 4. Its characteristic distribution is as follows:

(1) The overall change characteristics of AE event rate and cumulative event number: the AE event rate shows a "rise-drop-rise-drop" trend with the change of axial stress, and the cumulative event number of AE increases linearly; The AE event rate of $QSY_X$ is inverted "*M*" shape, $QSY_Z$ is inverted "*U*" shape, $FSY_X$ is inverted "*V*" shape, and $FSY_Z$ is irregular "*U*" shape.

(2) Variation characteristics of AE event rate at different stages: AE event rate of four kinds of sandstone can be divided into three stages, in which stage I corresponds to compaction stage, stage II corresponds to elastic deformation stage, and stage III correspond to plastic deformation stage. $QSY_X$: at stage I, due to the existence of micro defects and pores in the sample, compaction occurs during loading, and AE event rate develops from low to high. At stage II, due to the increase of sample compactness, it shows certain elastic characteristics, and the internal microcracks are developed and expand in the whole sample. At stage III, the internal cracks of the sample expanded faster and there is a connection, which has made the event rate slowly decline. After reaching the peak stress of 46.92 MPa, a sudden drop occurs, and the sample is unstable and damaged. $QSY_Z$: at stage I, as there are few micro defects in the sample, the event rate changes slowly, and only pores are compressed during the loading process. At stage II, under continuous load, the internal compactness of the sample reaches the bearing limit, and microcracks are formed and propagated. At stage III, microcrack growth and propagation have accelerated. When the peak stress reaches 43.32 MPa, the event rate drops suddenly and the sample is damaged. $FSY_X$: at stage I, similar to $QSY_X$. With the continuous loading of the sample, the internal micro defects and pores are compacted, and the event rate develops from low to high. At stage II, due to the increase of compactness, microcracks are formed inside the sample under continuous load, and the event rate changes from high to low to high. At stage III, the crack expansion and penetration speed up, AE event rate is the continuous change of high and low events. When reaching the peak strength of 57.87 MPa, the event rate decreases, and the sample breaks. $FSY_Z$: at stage I, the change of the event rate of the sample is similar to that of $QSY_Z$, with micro defects and pore compaction. At stage II, the sample pores and micro defects are compacted, and new cracks grow and expand under continuous load, and the event rate develops from high to low. At stage III, microcracks develop and expand faster, and there is connectivity, which makes the event rate change from low to high to low. After reaching the peak stress of 54.31 MPa, a sudden drop occurs and the sample is damaged.

(3) Characteristics of missing AE event rate: There are two reasons for missing AE event rate: (a) Closure of primary defects; (b) Signs of destruction. There are similarities and differences in the missing characteristics of the event rates of the four samples:

Similarity: AE event rate loss is located in front of the peak stress, where acoustic emission is extremely active. With the rapid expansion of macro cracks, failure and instability occur after reaching the peak stress, and the event rate loss phenomenon disappears.

Difference: AE event rate has different missing area, missing parts and missing numbers. $QSY_X$ event rate has larger missing area than $QSY_Z$ and $FSY_Z$, and the macro crack growth speed is relatively fast, with more obvious fracture signs. The number of $FSY_X$ event rate defects is more than that of $QSY_X$, $QSY_Z$ and $FSY_Z$. The first two defects are the closure of internal defects of the sample, and the last two defects are the sign of sample fracture.

*3.2.3. Analysis of AE Dominant Frequency Characteristics of Sandstone with Different Pores.* In the acoustic emission test, the original waveform can be formed by taking 2,048 sampling points as a sampling length. Because the original waveform will be interfered by many factors and contains many noises, the signal frequency with the highest amplitude is defined as the main frequency after the original waveform is processed by wavelet denoising threshold method, and the AE main frequency and axial stress evolution characteristic diagram with time are drawn after software calculation, as shown in Figure 5, The characteristic distribution is as follows:

(1) Overall change characteristics of AE dominant frequency: the distribution range of AE dominant frequency of the four samples is 0–240 kHz, which is in a strip distribution. It can be divided into low, medium and high frequencies in ascending order; AE dominant frequency signals are mainly concentrated in low frequency and high frequency, and intermediate frequency signals are relatively few. According to the AE high frequency and low-frequency proposed in literature [21], they correspond to the initiation of microcracks and the generation of large cracks respectively. It can be seen that $QSY_X$, $QSY_Z$ and $FSY_Z$ have more large cracks and fewer small cracks, while $FSY_X$ has fewer large cracks and more small cracks; According to the difference of distribution density of AE dominant frequency signal, AE dominant frequency can be divided into three stages, stage I (compaction stage), stage II (crack derivation and expansion stage) and stage III (failure and instability stage).

(2) Variation characteristics of AE dominant frequency in different stages: the three frequency bands of $QSY_X$ correspond to 0–42 kHz, 42–117 kHz and 117–240 kHz respectively. Low and high frequency signals are not interrupted during loading, and there are certain differences in the formation time of low, medium and high frequency aggregation. This frequency is the dominant frequency band in the sample fracture process; In stage I, there is no discontinuous signal in the high and low frequency bands, which indicates that the internal pores and micro defects of the sample will be compacted under the load, and some newly initiated microcracks will be formed. However, due to the large amount of signal loss in the high frequency band, there are few newly initiated microcracks penetrating; In stage II, the width of continuous signals in high and low frequency bands increases, accompanied by intermittent signals, and a large number of intermittent signals are also formed in the middle frequency band, which indicates that microcracks are steadily increasing. In stage III, the continuous signal width of the low frequency band narrows, the width of the high frequency band widens, and the intermediate frequency band forms a local continuous signal, and a large number of intermittent signals are formed in the three frequency bands at this stage. This indicates that the initiation of microcracks is accelerated and there is a phenomenon of convergence and penetration. When the peak stress is reached, they converge to form large cracks, and the sample is unstable and destroyed. The three frequency bands of $QSY_Z$ correspond to 0–59 kHz, 59–139 kHz and 139–235 kHz respectively. There is no interruption in the loading of low-frequency signals, and the medium and high-frequency signals are discontinuous signals. In stage I, the low-frequency band is a continuous signal without interruption, and the medium and high-frequency bands are a large number of discontinuous signals, which indicates that the internal pores and original defects of the sample are compacted, and a small number of primary fractures are penetrated locally, with a small scale. In stage II, the continuous and uninterrupted signal in the low frequency band remains, and the discontinuous signal in the medium and high frequency bands weakens, which indicates that there are new microcracks deriving and expanding in this stage. In stage III, a large number of discontinuous signals are formed in the three frequency bands, which indicates that the initiation and penetration of microcracks in the sample are accelerated at this stage, and a large number of uninterrupted signals are formed when the peak stress is reached. Microcracks converge into large cracks, and the sample is unstable and destroyed. The three frequency bands of $FSY_X$ correspond to 0–60 kHz, 60–142 kHz and 142–240 kHz respectively. The band signals are all local discontinuous and discontinuous. The high-frequency discontinuous area is the smallest, the intermediate frequency is the medium, and the low frequency is the largest. In stage I, the low-frequency band is a continuous signal, and the medium and high-frequency bands are discontinuous signals with local missing, which indicates that the samples at this stage are also mainly compacted by pores and microcracks. In stage II, the continuous signal in the low frequency band weakens to a discontinuous distribution, and the medium and high frequency

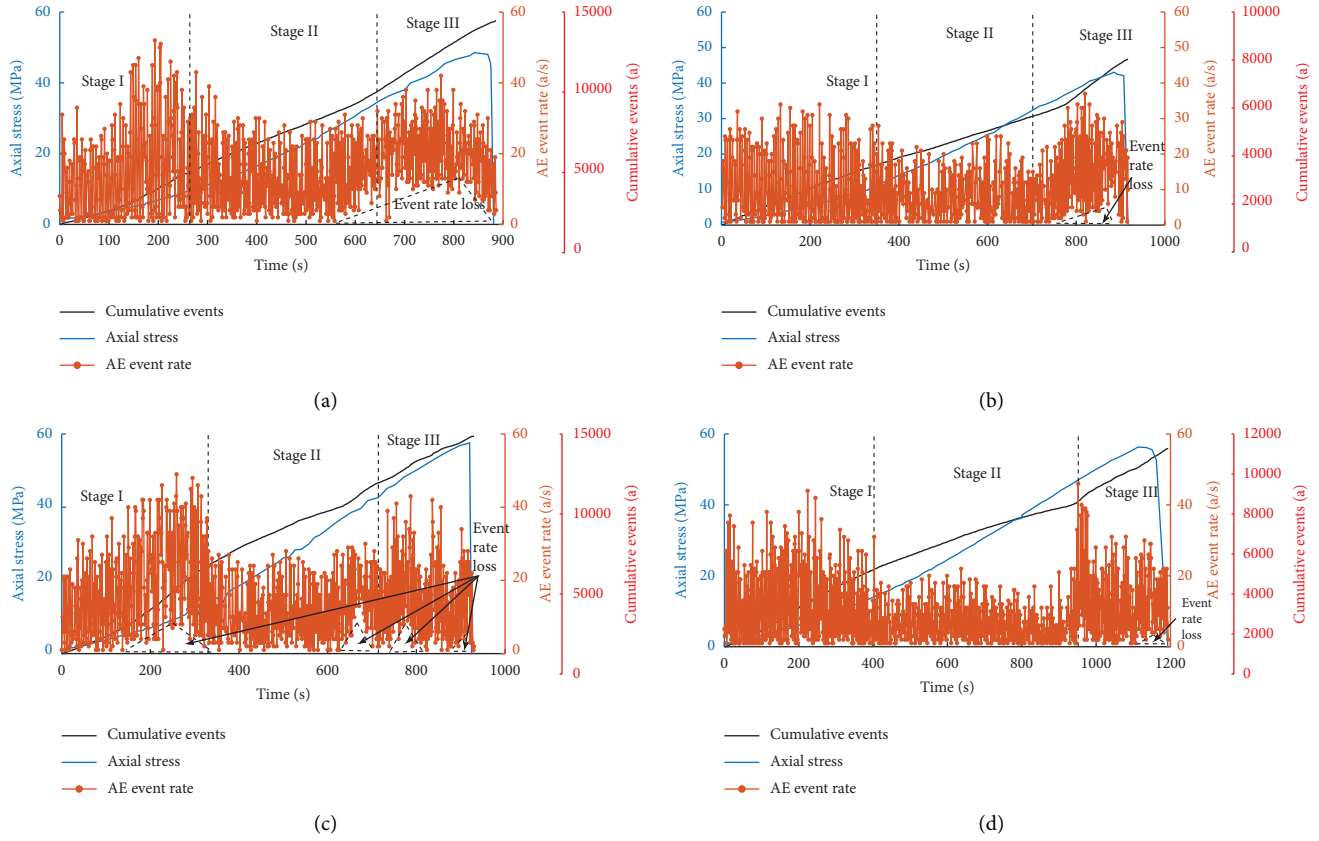


Figure 4: AE event rate-cumulative number of events-axial stress evolution over time. (a) $QSY_X$. (b) $QSY_Z$. (c) $FSY_X$. (d) $FSY_Z$.

bands change from local discontinuity to continuous distribution, and the signal amplitude in the high frequency band widens. This indicates that there are new crack initiation and propagation at this stage when the compactness of the sample increases to a certain extent. In stage III, the continuous signal in the high-frequency band remains the same, the scattered signal increases, and the signal in the medium and low-frequency bands decreases. This indicates that the specimen continues the initiation and propagation of the crack in the previous stage, but more shows the transformation from small crack to large crack. When the peak stress is reached, a large crack is formed and the sample is unstable. The three frequency bands of $FSY_Z$ correspond to 0–36 kHz, 36–132 kHz and 132–235 kHz respectively. The low and high frequency signals are continuous without interruption, and there are local dense signals in the intermediate frequency. Stage I, similar to $QSY_X$, mainly focuses on the compaction of pores and original defects, but there is a large area of signal loss in the high frequency band. Thus, there is also a small amount of new crack initiation. In stage II, the high and low frequency bands maintain continuous signals, and the samples mainly focus on the initiation and propagation of new cracks. However, there are many missing areas in the three frequency bands, which indicates that the penetration speed of new cracks in the samples is fast. In stage III, the scattered signals in the middle and high frequency bands suddenly increase, and the continuous signal width in the high frequency band increases, which indicates that the microcracks in the sample have gradually converged and penetrated to form large cracks. When the peak stress is reached, the sample will be unstable and destroyed.

*3.3. Analysis of Morphological Deterioration Characteristics of Sandstone with Different Pores.* The rock is mainly tensioned and sheared under external load, which will form a large number of AE time series characteristic signal parameters with fixed morphology. The RA-AF value of this parameter is used in the literature [16, 22–24] to characterize the expansion type of the internal cracks of the sample, and the expression is

$$\mathrm{RA} = \frac{\mathrm{Risetime}}{\mathrm{Amplitude}},$$
$$\mathrm{AF} = \frac{\mathrm{Counts}}{\mathrm{Duration}}, \tag{3}$$

where RA-ratio of rise time to amplitude, ms/V; AF-ratio of impact count to duration, kHz. When AF > RA, the failure type of the specimen is tensile failure, forming tensile cracks, and the energy generated is mainly stored in longitudinal waves. When AF < RA, it is shear failure and forms shear

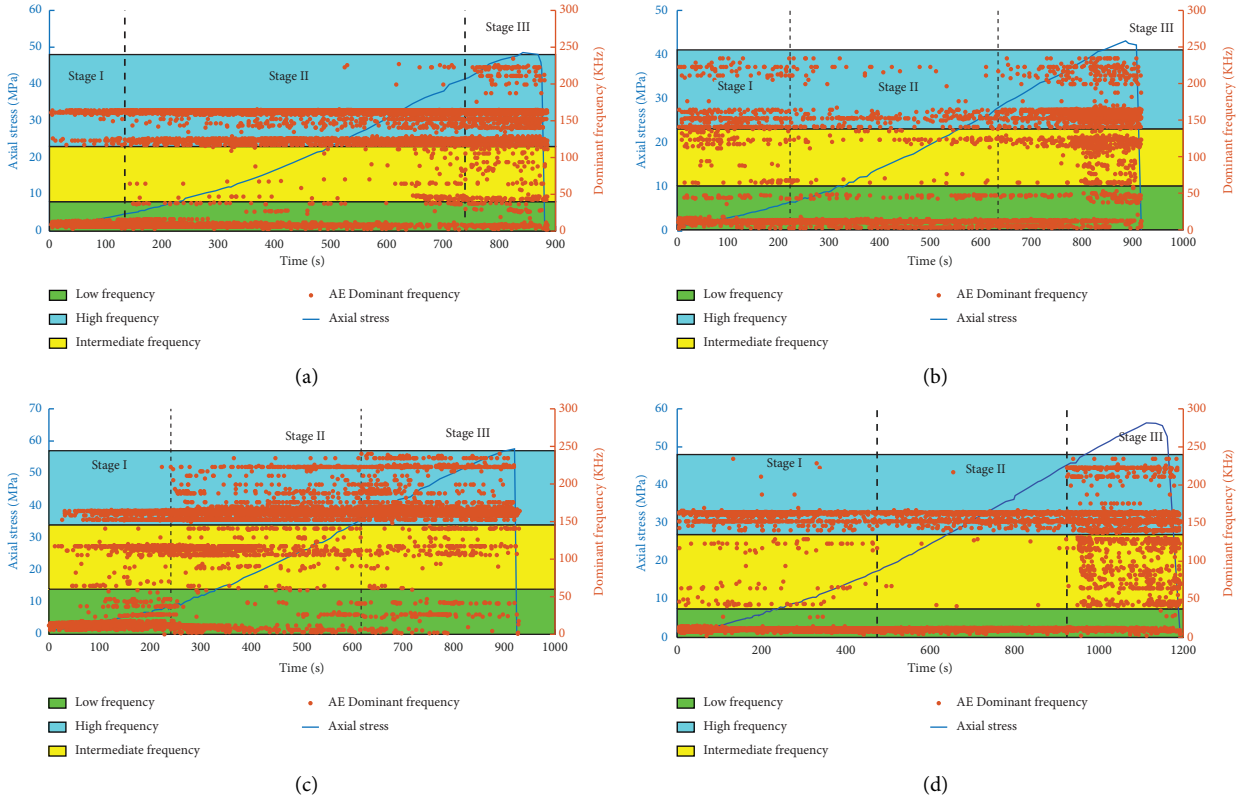


FIGURE 5: AE dominant frequency and axial stress evolution characteristics of sandstone with different pores over time. (a) $QSY_X$. (b) $QSY_Z$. (c) $FSY_X$. (d) $FSY_Z$.

crack. Literature [25, 26] proposed that the signals corresponding to tensile cracks have higher frequencies, whereas shear cracks have the opposite. From this, it can be seen that high AF and low RA values can represent the development of tensile cracks, and high RA and low AF values can represent the development of shear cracks. See Figure 6 for AE signal timing parameters and crack classification diagram. When AF > RA, the yellow area is tensile crack, and when AF < RA, the blue area is shear crack.

According to the method proposed in the literature [25, 26] and combined with the regional density statistical method, the RA-AF scattered points of four sandstone samples are divided into undifferentiated grids, and then the number of scattered points can be counted. After normalizing the dispersion of the statistical results by 0-1, the RA-AF scattered point distribution map is drawn, as shown in Figure 7. In Figure 7, 0 is the position with the sparsest scattered points (blue), and 1 is the position with the densest scattered points (red).

As shown in Figure 7, the RA-AF value distribution range of the four sandstone samples is the same, with an RA value of 0–500 ms/V and an AF value of 0–250 kHz. $QSY_X$, $QSY_Z$, and $FSY_Z$ are located in the red and orange areas of the shear fracture area, with a standardized density of more than 0.6. Although there is some orange and yellow in the tension fracture area, the proportion is smaller than that in the shear fracture area, and the RA-AF distribution characteristics of $FSY_X$ are more uniform. There are different distributions in the shear and tension fracture areas, but the red area in the tension fracture area is relatively large and concentrated, while the shear fracture area is mainly orange and light blue, and the standardized density is below 0.4. It can be seen that $QSY_X$, $QSY_Z$, and $FSY_Z$ are mainly damaged by shear and $FSY_X$ by tension under load, as shown in Figure 8.

## 4. Analysis of Damage Evolution and Critical Damage Value of Sandstone with Different Porosity under External Load

*4.1. Cellular Automaton.* Cellular automaton (CA) is a dynamic modeling method used by Von Neumann, the founder of computer and a famous mathematician in the United States, in the 1950s to simulate the self-organization evolution process of a discrete dynamic system caused by strong nonlinear interaction between internal units. It can simulate the spatiotemporal evolution process of complex systems and is composed of four parts: cell, cell space, cell neighbor, and cell rule. Common cell models include triangular mesh, tetragonal mesh, and hexagonal mesh [27], as shown in Figure 9.

*4.2. Establishment of Sandstone Cell Model and Determination of Critical Damage.* In recent years, with the rapid development of computer technology, many scholars have introduced cellular automata into the study of rock damage and deformation based on fractal theory. As a quantitative

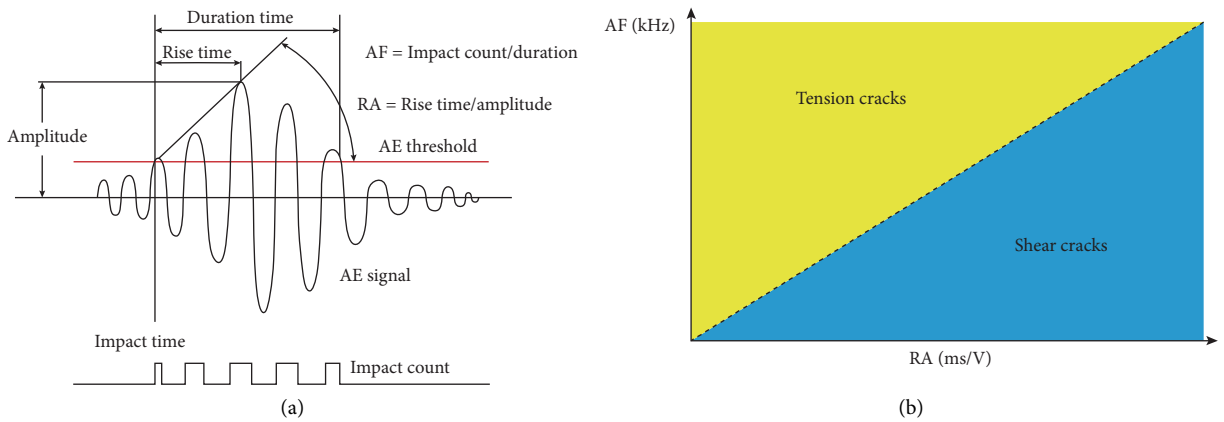


Figure 6: AE signal timing parameters and crack types. (a) AE signal timing parameters. (b) Crack classification.

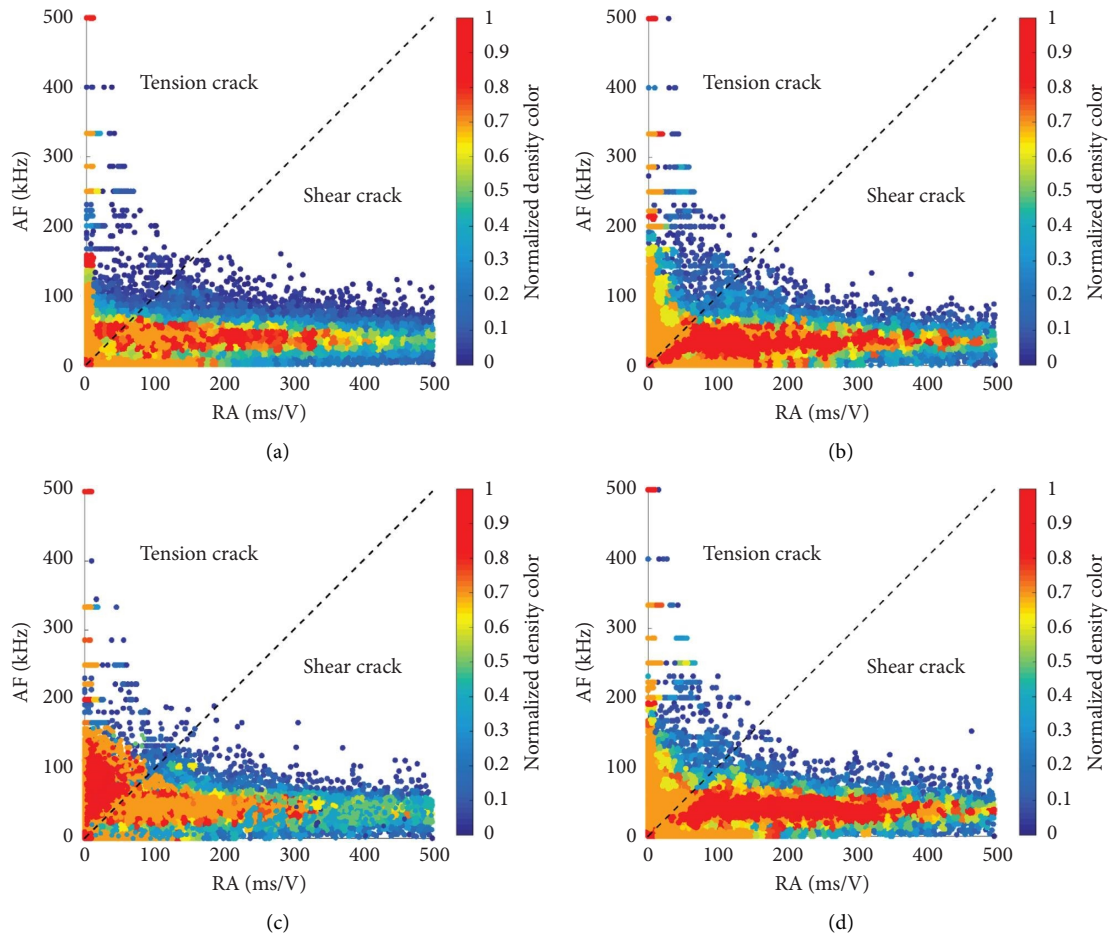


Figure 7: RA-AF distribution of AE signal timing parameters. (a) $QSY_X$. (b) $QSY_Z$. (c) $FSY_X$. (d) $FSY_Z$.

description of the degree of rock deterioration, damage can be expressed as $0 \le D \le 1$. When $D = 0$, it is in a non-destructive state; when $0 < D < 1$, it changes from non-destructive to damage deterioration; and when $D = 1$, it is completely damaged. Under the external load, the internal particles of rock will be destroyed randomly, and the damaged particles will form a new force on the surrounding particles, causing other particles to be destroyed until the rock is unstable and fractured. This phenomenon is more consistent with the failure of microelements in the cellular automata model. Therefore, on the basis of the above analysis, the sandstone cellular automata model with Moore type tetragonal grid is established by combining Weibull distribution function. First, it is assumed that the damage occurs at a certain section under external load; second, the section is divided into mesh elements according to the cell

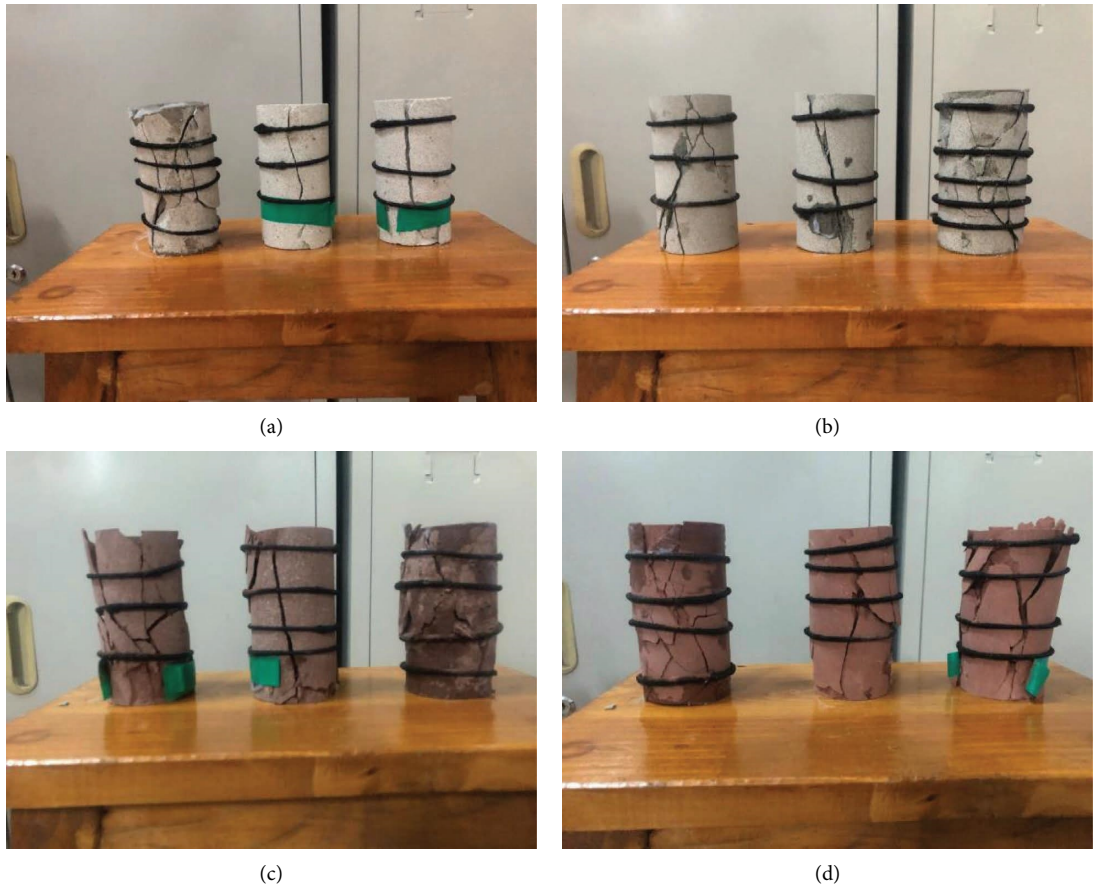


Figure 8: Failure characteristics of sandstone samples with different particle sizes. (a) $QSY_X$. (b) $QSY_Z$. (c) $FSY_X$. (d) $FSY_Z$.

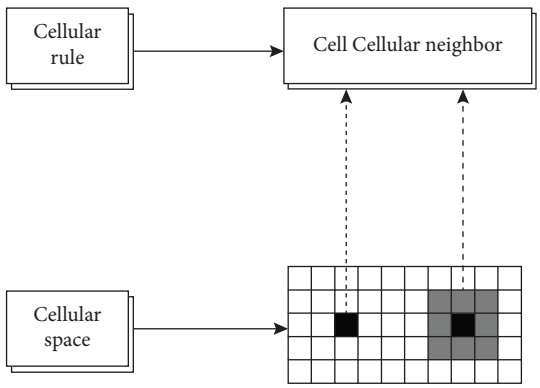


Figure 9: Cellular automata composition diagram.

space; and finally, each mesh divided is set as a cell. See Figure 10 for Moore type tetragonal grid cell model.

As shown in Figure 10, a section of the sandstone cell model is divided into $3n \times 3n$ grid elements, assuming: (a) the established cell element is subjected to the same force (Figure 11), when it is greater than the maximum load borne by the cell element, it will be damaged, and the force will continue to transfer to the adjacent element, and if three adjacent elements are damaged at the same time during the transfer process, it can be judged that this level of element is damaged; (b) the failure probability of each element obeys the distribution law of Weibull function; (c) the damage value $D$ is the failure probability $P_n$ of the unit under load, and the total failure probability is $P(F)$.

According to the cell renormalization method, a sandstone cell neighbor model with 9 cell scales is constructed. Nine first-order cell units form a second-order cell, nine second-order cells form a third-order cell, and so on. It goes in cycles and is constantly reconstructed. See Figure 12.

According to the above analysis, the failure of a cellular unit under the action of force F can be divided into two parts. The first part is the failure probability of the cell itself, expressed as $P$, and the second part is the diffusion probability transmitted by the failure cell, expressed as $P_m$. The probability that the first part of the cell will not be destroyed is $1 - P$. Therefore, according to the renormalization principle, the failure classification of the sandstone cell model can be calculated by using the Python language design program. The computed results are listed in Table 2.

From the above table, it can be concluded that the damage probability of level 1 cells is

(1) Probability of all 9 units intact

$$P(F)_1 = (1 - P)^9. \tag{4}$$

Cell failure probability

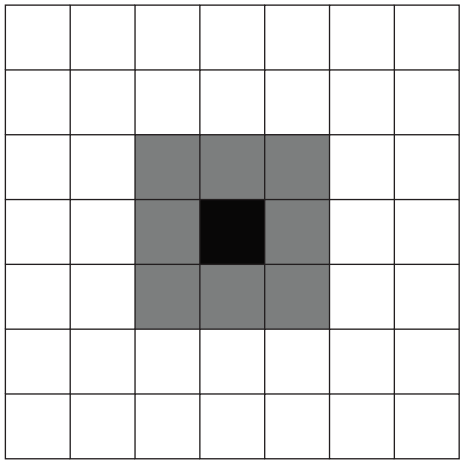

Figure 10: Cellular neighbor model.

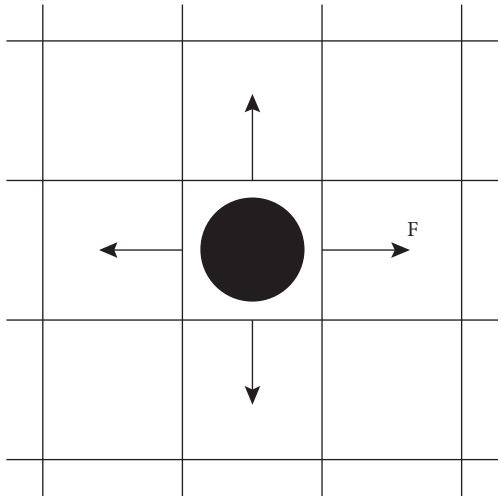


Figure 11: Stress model diagram of cellular unit.

$$P_1 = 0. \tag{5}$$

(2) Probability of one failure in 9 units

$$P(F)_2 = 9P(1-P)^8. \tag{6}$$

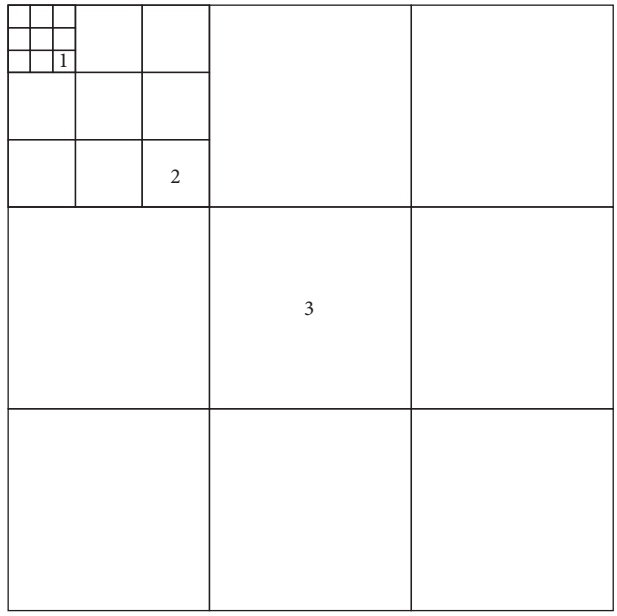


Figure 12: Renormalization of cellular units.

Probability of damage after diffusion

$$P(F)_2 = 9P(1-P)^8 24P_m. \tag{7}$$

Probability of cell failure

$$P_2 = P_1 + P(F_1)_2. \tag{8}$$

And so forth...

(3) Probability of 9 failure of 9 units

$$P(F)_{10} = P^9. \tag{9}$$

Cell failure probability

$$P_{10} = P(F)_{10}. \tag{10}$$

Through the above calculation, the total probability of cell failure under the action of force can be obtained

$$\begin{aligned} P(F) = {} & P_1 + P_2 + P_3 + P_4 + P_5 + P_6 + P_7 + P_8 + P_9 + P_{10} = 68P^5\,(P-1)^6 - 16P^2\,(P-1)^7 - 120P^4\,(P-1)^5 \\ & + 125P^5\,(P-1)^4 - 84P^6\,(P-1)^3 + 36P^7\,(P-1)^2 + P^9 - 9P^8(P-1) + 216PP_m\,(P-1)^8 - 12P_m\Big[120P^4\,(P-1)^5 \\ & + 360P^4P_m(P-1)^5\Big](P-1)^4 - 1440P^2P_m\,(P-1)^7 + 2496P^3P_m(P-1)^6 - 360P^4P_m(P-1)^5. \end{aligned} \tag{11}$$

The formula (11) is solved according to the calculation method in literature [28], and the following is obtained:

$$P = 0, 1, 0.078, 0.43. \tag{12}$$

According to the fixed point theorem, 0 and 1 are stable fixed points, so 0.078 and 0.43 can be determined as unstable fixed points. However, since 0.078 is close to 0, it can be attributed to fixed point 0, and $D = 0.43$ can be determined as the critical damage value of sandstone. At that time, the cells are in an unstable state, and instability and failure will occur at any time with the continuous load.

Table 2: Cellular unit destruction model classification table.

| Number of damaged cells | Number of damaged conditions | Number of cases not damaged | Number of adjacent damaged cells of stress diffusion cell | | | |
|---|---|---|---|---|---|---|
| | | | 1 | 2 | 3 | 4 |
| 0 | 0 | 1 | 0 | 0 | 0 | 0 |
| 1 | 0 | 9 | 24 | 0 | 0 | 0 |
| 2 | 16 | 20 | 60 | 22 | 0 | 0 |
| 3 | 68 | 16 | 28 | 36 | 8 | 0 |
| 4 | 120 | 6 | 0 | 16 | 8 | 1 |
| 5 | 125 | 1 | 0 | 0 | 4 | 0 |
| 6 | 84 | 0 | 0 | 0 | 0 | 0 |
| 7 | 36 | 0 | 0 | 0 | 0 | 0 |
| 8 | 9 | 0 | 0 | 0 | 0 | 0 |
| 9 | 1 | 0 | 0 | 0 | 0 | 0 |

*4.3. Damage Evolution and Critical Damage Determination of Sandstone with Different Pores.* The damage evolution process of different sandstones under external loads is essentially the initiation, propagation, and penetration of cracks. Literature [29, 30] points out that the damage strength of microelements obeys the Weibull function distribution law, that is

$$\varphi(\varepsilon) = \frac{\mathrm{m}}{\alpha}\varepsilon^{m-1}\exp\left(-\frac{\varepsilon^m}{\alpha}\right), \tag{13}$$

where $\varepsilon$ refers to the strain value of the sample, $m$ refers to the shape parameter of the sample, $\alpha$ refers to the scale parameter of the sample, and $\varphi(\varepsilon)$ refers to the unit damage rate. Literature [29, 30] pointed out that the deformation and failure of the sample can be expressed by the damage amount, from which the relationship between the damage variable and the damage rate of the microunit can be deduced, that is

$$\varphi(\varepsilon) = \frac{dD}{d\varepsilon}. \tag{14}$$

When equations (13) and (14) are combined, it can be obtained that

$$D = \int_0^{\varepsilon}\varphi(x)\mathrm{d}x = 1 - \exp\left(-\frac{\varepsilon^m}{\alpha}\right). \tag{15}$$

Literature [30] pointed out that the number of AE events derived from the specimen under external load can well reflect the change range of damage variables, namely $0 \le D \le 1$. If $W_m$ is to be taken as the cumulative event number of the sandstone sample, $W$ is the cumulative event number of failure when the stress is $\varepsilon$, including

$$W = W_m\int_0^{\varepsilon}\varphi(x)\mathrm{d}x. \tag{16}$$

When equations (15) and (16) are combined, the following formula can be obtained:

$$\frac{W}{W_m} = 1 - \exp\left(-\frac{\varepsilon^m}{\alpha}\right). \tag{17}$$

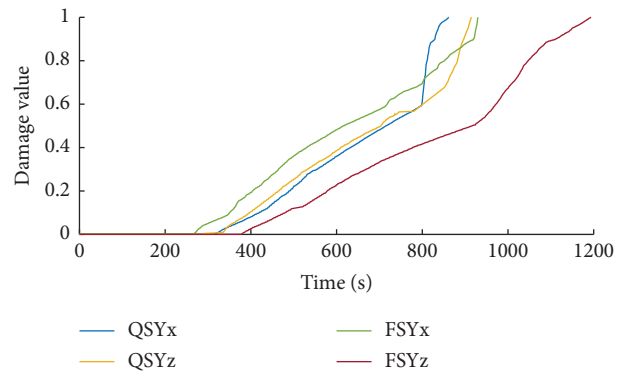


Figure 13: Damage evolution process of sandstone with different porosity.

The critical damage value of different sandstones under the same load can be obtained by combining equations (15) and (17), which can be expressed as

$$\frac{W}{W_m} = D. \tag{18}$$

Through the above description of $W_m$ and $W$, $W_t$ can be taken as the cumulative number of events (cumulative ringing count) when the loading duration is $t$ and $D_t$ is the corresponding damage value, that is

$$D_t = \frac{W_t}{W_m}. \tag{19}$$

It can be seen from above that $W_m$ is the cumulative number of events of the sample under external load, and $W$ is the cumulative number of events of failure of the sample when the stress is $\varepsilon$. Therefore, according to equations (18) and (19), the critical damage value and damage evolution process of different sandstones can be obtained. See Figure 13 for the damage evolution process of different sandstones.

It can be seen from Figure 13 that the damage evolution process of the four different pore sandstones can be divided into three stages: the damage quiescence stage, the damage expansion stage, and the damage acceleration stage, which

Table 3: Critical damage table of sandstone with different pores.

| Lithology | Cumulative events ($W_m$) | Cumulative events of damage ($W$) | Critical damage value ($D$) |
|---|---|---|---|
| $QSY_X$ | 12,140 | 5,318 | 0.438 |
| $QSY_Z$ | 12,400 | 6,188 | 0.499 |
| $FSY_X$ | 14,799 | 8,524 | 0.576 |
| $FSY_Z$ | 11,183 | 5,323 | 0.476 |

correspond to the compaction stage, elastic deformation stage, and plastic deformation stage of AE signal characteristics.

Damage quiescence stage: the damage value of the four samples approaches zero.

Damage expansion stage: the damage value of the four samples increases with the increase of microcracks and gradually increases from zero until the microcracks converge and penetrate. The damage reaches the critical value, which is 0.438, 0.499, 0.576, and 0.476, respectively (Table 3), which is larger than the critical damage value of the sandstone cell model of 0.43. It indicates that when the damage value of the four sandstone samples reaches the critical value, instability and failure will occur with the continuous load. Damage acceleration stage: due to irreversible deformation in the previous stage, the damage values of the four samples will continue to increase under continuous loading until the peak stress is reached. With the stress decay, the samples will be destabilized and destroyed, and the final damage value will become 1.

## 5. Conclusions

(1) Through nuclear magnetic resonance detection, it is found that the pore sizes of the four sandstones are $QSY_X > QSY_Z > FSY_X > FSY_Z$. Large and small pores coexist in $QSY_X$, $FSY_X$, and $FSY_Z$, and $QSY_Z$ is dominated by large pores. The loading process of the four sandstones can be divided into three stages: compaction, elastic deformation, and plastic deformation, with peak strengths of 46.92 MPa, 43.32 MPa, 57.87 MPa, and 54.31 MPa, respectively. The AE event rate of $QSY_X$ is an inverse "*M*" type, $QSY_Z$ is an "*U*" type, $FSY_X$ is an inverse "*V*" type, and $FSY_Z$ is an irregular "*U*" type. The AE energy rate trend is "rising-falling-rising," and the overall shape is similar to "*U*" type. The main frequency of AE is distributed in strips in ascending order of low frequency, medium frequency, and high frequency. $QSY_X$, $QSY_Z$, and $FSY_Z$ are dominated by large cracks, and $FSY_X$ is dominated by small cracks;

(2) According to the two reasons for the missing AE event rate, it can be known that the missing AE event rate of the four samples is located before the peak stress, and after reaching the peak stress, the missing event rate disappears. The area of $QSY_X$ deletion is larger than that of $QSY_Z$ and $FSY_Z$; the macrocrack expansion speed is also relatively fast; and the fracture sign is more evident. The number of $FSY_X$ deletions is more than that of $QSY_X$, $QSY_Z$, and $FSY_Z$. The first two deletions are the closure of internal defects of the sample, and the last two deletions are the fracture signs of the sample;

(3) According to the AE signal timing parameters, the RA-AF values of the four samples all have the same distribution range. The RA value is 0–500 ms/V, and the AF value is 0–250 kHz. $QSY_X$, $QSY_Z$, and $FSY_Z$ are located in the red and orange areas of the shear fracture area, accounting for a large proportion. The normalized density is above 0.6, which is a shear failure. The red area of $FSY_X$ RA-AF in the tensile fracture area accounts for a large proportion and is concentrated. The shear fracture area is mainly orange and light blue. The normalized density is below 0.4, which is a tensile failure;

(4) The damage evolution process of the four sandstone samples with different pores corresponds to the loading process one by one. At the stage of damage quiescence, the damage values of the four sandstone samples all approach zero. In the damage expansion stage, the critical damage values are 0.438, 0.499, 0.576, and 0.476, which are all larger than the critical damage value of the sandstone cell model (0.43). It can be concluded that instability exists when the samples reach the critical damage value. In the damage acceleration stage, due to the irreversible deformation in the previous stage, after reaching the peak stress, the specimen will be unstable and damaged with the stress decay, and the final damage value will become 1.

## Data Availability

The data included in this study are available from the corresponding author upon request.

## Conflicts of Interest

The authors declare that they have no conflicts of interest.

## Authors' Contributions

W. W. conceptualized the study; J. L. was in charge of methodology; C. W. and J. L. were in charge of investigation; J. L. handled data curation; J. L. and Z. P. were in charge of formal analysis; J. L. handled validation; J. L. was in charge of writing the original draft; and J. L. was in charge of writing the review and editing. All authors read and agreed to the published version of the manuscript.

## Acknowledgments

This research presented in this paper was funded by the National Natural Science Foundation of China (grant nos. 60171009, 51764044, and 51464036) and the Natural Science Foundation of Neimenggu Province of China (grant nos. 2020MS05010 and 20180823).

## References

[1] C. B. Scruby, "An introduction to acoustic emission," *Journal of Physics E Scientific Instruments*, vol. 20, no. 8, pp. 946–953, 1987.

[2] X. You, B. Gong, X. Lv, and L. Hu, "Study on the mathematical model and propagation characteristics of AE waveform signals during rock fracture," *Advances in Civil Engineering*, vol. 2021, Article ID 6685357, 13 pages, 2021.

[3] S. Q. Yang, H. W. Jing, Y. S. Li, and L. J. Han, "Experimental investigation on mechanical behavior of coarse marble under six different loading paths," *Experimental Mechanics*, vol. 51, no. 3, pp. 315–334, 2011.

[4] L. R. Li, J. H. Deng, L. Zheng, and J. F. Liu, "Dominant frequency characteristics of acoustic emissions in white marble during direct tensile tests," *Rock Mechanics and Rock Engineering*, vol. 50, no. 5, pp. 1337–1346, 2017.

[5] X. B. Li, W. Z. Cao, Z. L. Zhou, and Y. Zou, "Influence of stress path on excavation unloading response," *Tunnelling and Underground Space Technology*, vol. 42, pp. 237–246, 2014.

[6] J. P. Liu, Y. H. Li, S. D. Xu, S. Xu, C. Y. Jin, and Z. S. Liu, "Moment tensor analysis of acoustic emission for cracking mechanisms in rock with a pre-cut circular hole under uniaxial compression," *Engineering Fracture Mechanics*, vol. 135, pp. 206–218, 2015.

[7] D. Lockner, "The role of acoustic emission in the study of rock frac-ture," *International Journal of Rock Mechanics and Mining Sciences & Geomechanics Abstracts*, vol. 30, no. 7, pp. 883–899, 1993.

[8] G. Manthei, "Characterization of acoustic emission sources in a rock salt specimen under triaxial compression," *Bulletin of the Seismological Society of America*, vol. 95, no. 5, pp. 1674–1700, 2005.

[9] C. P. Lu, L. M. Dou, H. Liu, H. S. Liu, B. Liu, and B. B. Du, "Case study on microseismic effect of coal and gas outburst process," *International Journal of Rock Mechanics and Mining Sciences*, vol. 53, no. 5, pp. 101–110, 2012.

[10] Z. Zhang, R. Zhang, H. Xie, J. Liu, and P. Were, "Differences in the acoustic emission characteristics of rock salt compared with granite and marble during the damage evolution process," *Environmental Earth Sciences*, vol. 73, no. 11, pp. 6987–6999, 2015.

[11] S. Q. Yang and H. W. Jing, "Strength failure and crack coalescence behavior of brittle sandstone samples containing a single fissure under uniaxial compression," *International Journal of Fracture*, vol. 168, no. 2, pp. 227–250, 2011.

[12] E. Eberhardt, D. Stead, and B. Stimpson, "Quantifying progressive pre-peak brittle fracture damage in rock during uniaxial compression," *International Journal of Rock Mechanics and Mining Sciences*, vol. 36, no. 3, pp. 361–380, 1999.

[13] N. Erarslan and D. J. Williams, "Experimental, numerical and analytical studies on tensile strength of rocks," *International Journal of Rock Mechanics and Mining Sciences*, vol. 49, pp. 21–30, 2012.

[14] D. Li and L. N. Y. Wong, "The brazilian disc test for rock mechanics applications: review and new insights," *Rock Mechanics and Rock Engineering*, vol. 46, no. 2, pp. 269–287, 2013.

[15] S. Invernizzi, G. Lacidogna, and A. Carpinteri, "Particle-based numerical modeling of AE statistics in disordered materials," *Meccanica*, vol. 48, no. 1, pp. 211–220, 2013.

[16] Z. H. Zhang and J. H. Deng, "A new method for determining the crack classification criterion in acoustic emission parameter analysis," *International Journal of Rock Mechanics and Mining Sciences*, vol. 130, Article ID 104323, 2020.

[17] X. Wu, J. Liu, and X. Liu, "Study on the coupled relationship between AE accumulative ring-down count and damage constitutive model of rock," *Journal of Mining & Safety Engineering*, vol. 32, no. 1, pp. 28–34, 2015.

[18] X. B. Gu, W. Y. Guo, C. G. Zhang et al., "Mechanical behaviors and AE characteristics of brittle coal specimens with different fissure angles," *Geofluids*, vol. 2022, Article ID 4093526, 13 pages, 2022.

[19] J. L. Li and K. Q. Zhou, "Experimental study of rock porous structure damage characteristics under condition of freezing-thawing cycles based on NUCLEAR magnetic resonance technology," *Chinese Journal of Rock Mechanics and Engineering*, vol. 31, no. 6, pp. 1208–1214, 2012.

[20] F. Pei, H. G. Ji, J. W. Zhao, and J. Geng, "Energy evolution and AE failure precursory characteristics of rocks with different rockburst proneness," *Advances in Civil Engineering*, vol. 2020, Article ID 8877901, 12 pages, 2020.

[21] M. Cai, P. K. Kaiser, H. Morioka et al., "FLAC/PFC coupled numerical simulation of AE in large-scale underground excavations," *International Journal of Rock Mechanics and Mining Sciences*, vol. 44, no. 4, pp. 550–564, 2007.

[22] M. Ohtsu, *Innovative AE and NDT Techniques for On-Site Measurement of concrete and Masonry Structures*, Springer, Dordrecht, Netherlands, 1st edition, 2016.

[23] A. Carpinteri, G. Lacidogna, F. Accornero, A. Mpalaskas, T. Matikas, and D. Aggelis, "Influence of damage in the acoustic emission parameters," *Cement and Concrete Composites*, vol. 44, pp. 9–16, 2013.

[24] D. G. Aggelis, D. V. Soulioti, N. Sapouridis, N. Barkoula, A. Paipetis, and T. Matikas, "Acoustic emission characterization of the fracture process in fibre reinforced concrete," *Construction and Building Materials*, vol. 25, no. 11, pp. 4126–4131, 2011.

[25] H. R. Nejati, A. Nazerigivi, and A. R. Sayadi, "Physical and mechanical phenomena associated with rock failure in Brazilian Disc Specimens," *International Journal of Environmental, Chemical, Ecological, Geological and Geophysical Engineering*, vol. 12, no. 1, pp. 35–39, 2018.

[26] D. G. Aggelis, "Classification of cracking mode in concrete by acoustic emission parameters," *Mechanics Research Communications*, vol. 38, no. 3, pp. 153–157, 2011.

[27] Z. T. Ma and Y. L. Tan, "Simulation study of rock failure based on MH-PCA model," *Chinese Journal of Rock Mechanics and Engineering*, vol. 24, no. 15, pp. 2704–2708, 2005.

[28] S. L. Li and Q. C. Zhang, "Theoretical Study and SHPB experimental verification on the critical damage of uniform sandstone," *Journal of Beijing Institute of Technology (Social Sciences Edition)*, vol. 37, no. 8, pp. 807–812, 2017.

[29] H. B. Zhao and G. Z. Yin, "Study of acoustic emission characteristics and damage equation of coal containing gas," *Rock and Soil Mechanics*, vol. 32, no. 3, pp. 29–32, 2011.

[30] Z. H. Chen and G. H. Tan, "Renormalization study and numerical simulation on brittle failure of rocks," *Chinese Journal of Geotechnical Engineering*, vol. 24, no. 2, pp. 184–187, 2002.